

■ Medicinal Chemistry & Drug Discovery

Bis(thio)carbohydrazone Luminogens with AIEE and ACQ Features and Their *In Silico* Investigations with SARS-CoV-2

K. K. Mohammed Hashim, E. Manoj,* and M. R. Prathapachandra Kurup*^[a]

Herein, we report two novel multidentate luminogen proligands bis(3,5-diiodosalicylidene) carbohydrazone (H_4L^1) and bis(3,5-diiodosalicylidene) thiocarbohydrazone (H_4L^2), which are suitable candidates for biomedical applications. Though the thiocarbohydrazone H_4L^2 shows aggregation caused quenching (ACQ), the carbohydrazone H_4L^1 exhibits stronger fluorescence due to aggregation induced emission enhancement (AIEE). Molecular docking studies of H_4L^1 and H_4L^2 along with four similar (thio)carbohydrazones with the active sites of SARS-CoV-2 main protease 3CL^{pro} reveals that the thiocarbohydra-

zones, in general, are showing better propensity compared to their oxygen analogues. Both the thiocarbohydrazones and the carbohydrazones, however, exhibit better binding potential at the active sites than that of some of the repurposed drugs such as chloroquine, hydroxychloroquine, lopinavir, ritonavir, darunavir and remdesivir. Also, the carbohydrazone H_4L^1 can be a better bioprobe compared to H_4L^2 as the former is found to have better binding potential with SARS-CoV-2 spike glycoprotein along with AIEE feature.

Introduction

Bioactive compounds showing aggregation induced emission (AIE) features offer huge opportunities for the analysis of bioactive species and for monitoring complicated biological processes.^[1] AIE phenomenon has attracted tremendous research interest in the scientific community due to wide range of applications such as chemosensors, biomedical imaging, photodynamic therapy, optoelectronic devices, etc.^[1–7] Conventional luminescence probes encounter aggregation caused quenching (ACQ) problems and are thus limited in usage. Development of AIE in the field of biomedicine has brought huge opportunities for the analysis of bioactive species, diagnosis of diseases by monitoring complicated biological processes, and the elucidation of key physiological and pathological behaviors.^[1,8] Several mechanisms of AIE have been proposed, which mainly involve restricted intramolecular rotations (RIR), restricted intramolecular vibrations (RIV), restricted twisted intramolecular charge transfer (TICT), *cis/trans* isomerization, etc.^[4,5,9] Current long-term pandemic coronavirus disease 2019 (COVID-19), caused by the severe acute respiratory syndrome coronavirus 2 (SARS-CoV-2)^[10,11] completely threatens global public health and thus requires new sensitive and accurate AIEgen based bioprobes and novel drug candidates.

The novel coronavirus is a single stranded positive sense RNA similar to the SARS-CoV and MERS-CoV family and is responsible for the disease.^[12,13] The development of novel

therapeutics is also under investigation, though various mutations of coronaviruses are spreading. To overcome the dangerous contagious situation, scientists are looking for the repurposing of drugs like chloroquine (CQ), hydroxychloroquine (HCQ), ritonavir, lopinavir, darunavir, remdesivir etc.^[14–17] mainly to inhibit the viral chymotrypsin-like cysteine protease, also known as Main protease (3CL^{pro}).^[18] The active sites of the SARS-CoV enzyme 3CL^{pro} contain catalytic diad involving Cys145 and His41, in which the cysteine functions as a nucleophile and histidine as an acid/base catalyst in the proteolysis reaction.^[19,20] Therefore, the 3CL^{pro} is responsible for polyprotein maturation and is an ideal target for the discovery of therapeutic drugs against SARS-CoV-2.^[21–24] Various research is in progress in different directions, around the world, for the development of novel therapeutic drugs against COVID-19.^[15,25–27] Exploration of novel luminescence probes having binding potentials with SARS-CoV-2 can play a crucial role in improving the detection sensitivity of coronaviruses and thus such AIE materials, in particular, would be promising anti-COVID-19 weapons.

(Thio)carbohydrazones and their complexes have been reported to have a wide range of biological applications such as anti-viral, anti-fungal, anti-bacterial, anti-microbial, etc. in general and superior anti-cancer activity in particular.^[28–30] Computational modelling techniques, based on different structures and ligands for the design of novel inhibitors against coronavirus, can provide detailed but putative binding modes of the compounds within the 3CL^{pro} binding pockets. Molecular docking studies of bioactive thiosemicarbazones and their complexes, especially platinum and palladium, have revealed excellent binding potential with SARS-CoV-2 main protease.^[17,31] We recently have reported a bithiocarbohydrazone, a bioactive higher homologue of thiosemicarbazone, and its Mn(II) complex with better binding efficacy compared to CQ and HCQ.^[32] Herein, we report two novel luminogens, a bithiocar-

[a] K. K. Mohammed Hashim, E. Manoj, M. R. Prathapachandra Kurup
Department of Applied Chemistry,
Cochin University of Science and Technology,
Kochi, Kerala 682 022, India
E-mail: mrp@cusat.ac.in
manoj@cusat.ac.in

 Supporting information for this article is available on the WWW under
<https://doi.org/10.1002/slct.202201229>

bohydrazone and its oxygen analogue biscarbohydrazone. The compounds were characterized by analytical and spectroscopic methods along with the single crystal X-ray diffraction (SCXRD) of the biscarbohydrazone. The density functional theory (DFT) calculations were performed and the molecular docking studies were carried out to identify the binding efficacy of the proligands with SARS-CoV-2 main protease. Also, to understand and compare the frontier molecular orbital (FMO) and electronic features and the binding potentials of thiocarbohydrazones with carbohydrazones in general, selected (thio)carbohydrazone compounds 1,5-bis(di-2-pyridyl ketone) thiocarbohydrazone (H_2L^3)^[33,34], 1,5-bis(quinoline-2-carbaldehyde) thiocarbohydrazone (H_2L^4)^[34], 1,5-bis(di-2-pyridyl ketone) carbohydrazone (H_2L^5)^[34], and 1,5-bis(quinoline-2-carbaldehyde) carbohydrazone (H_2L^6)^[33,35], which are reported previously from our group, were also optimized by DFT method and their *in silico* molecular docking with the same protease are also carried out. Moreover, as the new compounds are exhibiting fluorescent ACQ and AIEE characteristics, finding their utility as novel bioprobes putative binding potentials with SARS-CoV-2 spike glycoprotein is also studied and reported.

Experimental

Materials

3,5-Diiodosalicylaldehyde (Aldrich), carbohydrazide (Aldrich), thio-carbohydrazide (Aldrich), methanol (Merck), DMSO (Spectrochem), glacial acetic acid (Spectrochem), etc. were used as received.

Syntheses of the proligands

Procedures for the synthesis of the proligands were adapted from previously reported works.^[28,33–35]

Synthesis of bis(3,5-diiodosalicylidene)carbohydrazone (H_4L^1)

A hot solution of 3,5-diiodosalicylaldehyde (1.53 g, 4.1 mmol) in 10 mL of methanol was added to a hot solution of carbohydrazide (0.1802 g, 2 mmol) in 10 mL methanol. After adding a drop of glacial acetic acid, the solution was refluxed for 2 hours, and on cooling a yellow mass precipitated. It was then filtered, washed with methanol and diethyl ether, and dried over P_2O_5 *in vacuo*. Single crystals suitable for X-ray diffraction were obtained by slow evaporation of a DMSO solution of H_4L^1 . Yield: 81%. CHN (calculated for $H_4L^1 \cdot H_2O$): Observed (calc.): C, 21.61 (21.97); H, 1.24 (1.48); N, 7.30 (6.83)%. ¹H NMR (400 MHz, DMSO- d_6) δ , ppm: 11.31 (2H, s, N–NH–C), 8.95 (2H, s, OH), 8.21 (2H, s, HC=N), 7.88–7.98 (4H, m, Ar–H). ¹³C NMR (100 MHz, DMSO- d_6) δ , ppm: 156.13 (C=O), 152.06 (C–O), 146.60 (C=N)_{azomethine}, 143.21, 138.03, 122.39, 89.26, 83.37 (aromatic carbons)^[36] (Figure S1). MALDI-MS *m/z* [Found (calc.)]: 825.044 (824.692) [M + Na]⁺.

Synthesis of bis(3,5-diiodosalicylidene)thiocarbohydrazone (H_4L^2)

A hot solution of 3,5-diiodosalicylaldehyde (1.14 g, 3.05 mmol) in 20 mL of methanol was added to a hot solution of thiocarbohydrazide (0.1592 g, 1.5 mmol) in 30 mL methanol. After adding a drop of glacial acetic acid, the solution was refluxed for 2 hours,

and on cooling a pale yellow mass precipitated. It was then filtered, washed with methanol and diethyl ether, and dried over P_2O_5 *in vacuo*. Yield: 90%. CHNS (calculated for $H_4L^2 \cdot H_2O$): Observed (calc.): C, 21.09 (21.55); H, 1.66 (1.45); N, 6.79 (6.70); S, 3.79 (3.84)%. ¹H NMR (400 MHz, DMSO- d_6) δ , ppm: 12.34 (2H, s, N–NH–C), 10.07 (2H, s, OH), 8.51 (1H, s, HC=N), 8.33 (1H, s, HC=N), 7.82–8.03 (4H, m, Ar–H)^[37] (Figure S2). MALDI-MS *m/z* [Found (calc.)]: 820.172 (818.678) [M + H]⁺.

Methods and Instrumentation

CHNS analysis of the compounds were carried out using an Elementar Vario EL III CHNS analyzer. MALDI mass spectra were taken using Bruker Autoflex spectrometer at Sophisticated Test and Instrumentation Centre (STIC), CUSAT, Kochi, India. ¹H NMR and ¹³C NMR spectra of the H_4L^1 and H_4L^2 were recorded using JEOL 400 MHz FTNMR (JNM-ECZ400S/L1) instrument at Government College for Women, Thiruvananthapuram, India. Electronic spectra (200–900 nm) were recorded on a UV-Thermo scientific evolution 220 spectrometer and the diffuse reflectance UV-visible spectra were recorded on Ocean Optics DH-2000-BAL instrument at the Department of Applied Chemistry (DAC), CUSAT, Kochi, India. Infrared spectra of the compounds in the range 4000–400 cm^{-1} were recorded on a JASCO FT-IR 4100 spectrometer with KBr pellets at the DAC. The fluorescence emission studies were conducted on a Horiba fluorolog 3 (FL-1057) Spectrofluorimeter at the DAC.

X-ray crystallography

The SCXRD study of the proligand H_4L^1 was carried out using Bruker SMART APEXII CCD diffractometer, equipped with a graphite crystal incident-beam monochromator, and a fine focus sealed tube with Mo K α ($\lambda = 0.71073$ Å) radiation as the X-ray source at the SAIF, STIC, Kochi, India. The unit cell dimensions were measured, and the data collection was performed at 296(2) K. The Bruker SMART software and Bruker SAINT software were used for data acquisition and data integration respectively.^[38] The structure was solved by direct methods and refined by full-matrix least-squares refinement on F^2 using SHELXL-2018/1 software package.^[39] Anisotropic refinements were performed for all non-hydrogen atoms, and all hydrogen atoms on carbon were placed in calculated positions, guided by difference map, and refined isotropically. Hydrogen atoms attached to the nitrogen atoms couldn't be located and are geometrically fixed. It contains two DMSO solvent molecules of which one is disordered over two positions with occupancies of 0.712(5) and 0.288(5) for major and minor components respectively. The disordered components were restrained to have the same bond lengths as the undisordered component by the SAME instruction. SIMU instruction was used to restrain the disordered components. The molecular and crystal structure was plotted using ORTEP^[40], PLATON^[41], Mercury^[42], and Diamond 3.2 k^[43] programs. The crystal data and structural refinement parameters of the proligand are given in Table 1 and the relevant bond lengths and bond angles are listed in Table S1 in the Supporting Information.

Computational study

The DFT calculations were performed using Gaussian 09 program package^[44] and GaussView 5.09 molecular visualization programs^[45] at the computational chemistry facility lab, DAC, CUSAT. Geometry optimizations and frequency calculations of the proligands were

Table 1. Crystal data and structure refinement parameters of H₄L¹.

CCDC number	2090512
Empirical Formula	C ₁₉ H ₂₂ I ₄ N ₄ O ₅ S ₂
Formula weight (M)	958.12
Temperature (T)	296(2) K
Wavelength (Mo K α)	0.71073 Å
Crystal system	monoclinic
Space group	<i>P</i> 2 ₁ / <i>c</i>
Unit cell dimensions	a = 12.4267(9) Å α = 90° b = 15.3730(16) Å β = 99.334(3)° c = 15.5694(16) Å γ = 90°
Volume V, Z	2934.9(5) Å ³ , 4
Calculated density (ρ)	2.168 mg/m ³
Absorption coefficient, μ	4.424 mm ⁻¹
<i>F</i> (000)	1792
Crystal size	0.300 × 0.250 × 0.200 mm
Limiting Indices	-19 ≤ <i>h</i> ≤ 9, -23 ≤ <i>k</i> ≤ 23, -24 ≤ <i>l</i> ≤ 22
Reflections collected	26550
Independent Reflections	10298 [R(int) = 0.0733]
Refinement method	Full-matrix least-squares on F ²
Data/restraints/parameters	11759/114/353
Goodness-of-fit on F ²	1.001
Final <i>R</i> indices [<i>I</i> > 2 σ (<i>I</i>)]	<i>R</i> ₁ = 0.0558, <i>wR</i> ₂ = 0.1174
<i>R</i> indices (all data)	<i>R</i> ₁ = 0.1490, <i>wR</i> ₂ = 0.1554
Largest difference peak and hole	1.047 and -1.148 e Å ⁻³

$$R_1 = \sum ||F_o| - |F_c|| / \sum |F_o|^n; wR_2 = [\sum w(F_o^2 - F_c^2)^2 / \sum w(F_o^2)^3]^{1/2}$$

conducted with a hybrid functional B3LYP level of theories using Becke's three-parameter nonlocal exchange function^[46] with the Lee-Yang-Parr correlation function^[47] at 6-311G (d,p) and LanL2DZ basis sets. H₄L¹ and H₄L² were optimized by taking LanL2DZ basis set for iodine and 6-311G (d,p) for other atoms. Relevant bond lengths and bond angles of H₄L¹ are listed along with the crystal data in Table S1.

Molecular docking study

The molecular docking simulations were performed using AutoDock Tool (ADT) version 1.5.6 software.^[48] The CIF format files or DFT optimized structures were converted to PDB files using mercury software. The 3D structure of the SARS-CoV-2 main protease (PDB ID: 6Y2F)^[49] and SARS-CoV-2 spike protein (PDB ID: 6MOJ)^[50] were obtained from the Protein Data Bank.^[51] The water molecules were removed from the enzyme and both protein and ligands were prepared in pdbqt format. The polar hydrogens and Gasteiger charges were added to the receptor and 50 runs were carried out using Lamarckian genetic algorithm to find the best

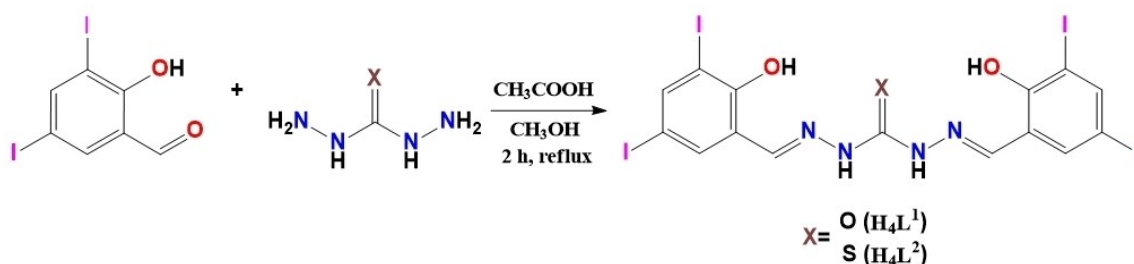
binding pose. Docked poses were visualized using Discovery studio^[52] and Pymol^[53] software.

Results and discussion

The compounds were synthesized by the condensation between 3,5-diiodosalicylaldehyde with carbohydrazide (H₄L¹) or thiocarbohydrazide (H₄L²) in methanol in the presence of a trace amount of acetic acid (Scheme 1). Both the proligands were found soluble in DMSO and DMF, insoluble in water and some of the organic solvents like chloroform, methanol, acetonitrile, dichloromethane, ethyl acetate, etc. H₄L² is soluble in THF on heating. Both the compounds were characterized by elemental analysis, MALDI-TOF MS, NMR, FT IR and UV-Visible solid state and solution phase spectra, and the structure of H₄L¹ is confirmed by SCXRD study.

Crystal structure of bis(3,5-diiodosalicylidene)carbohydrazone

Single crystals of the proligand H₄L¹ were obtained from its DMSO solution on slow evaporation and got crystallized in monoclinic *P*2₁/*c* space group with four molecules in the unit cell. The molecular structure and the relevant numbering scheme used for the proligand H₄L¹ with intramolecular hydrogen bonding is given in Figure 1. The C7-N1 and C9-N4 bonds confirm the formation of azomethine bonds and are at distances of 1.285(7) and 1.287(7) Å respectively. C7-N1-N2 and C9-N4-N3 bond angles of 120.0(5)° and 119.5(5)°, respectively suggest that the atoms C7, N1 and C9, N4 are sp² hybridized. Relevant hydrogen bonding interactions, significant $\pi \cdots \pi$ interactions, and a prominent C-H $\cdots \pi$ interaction found in the packing of the crystal lattice are listed in Table S2. The molecule shows two conventional intramolecular hydrogen bonding between O1-H1A \cdots N1 and O3-H3B \cdots N4 at a hydrogen-acceptor distance of 1.85 and 1.83 Å, respectively. The C8-O2 bond distance of 1.204(7) Å reveals that the proligand exists in its ketone tautomeric form.^[35] One of the two DMSO solvent present in the crystal lattice is engaged in C-H $\cdots \pi$ interaction involving C17-H17A and one of the phenylene rings (Figure S3). The phenylene rings of adjacent molecules form mutual $\pi \cdots \pi$ stacking interactions with a centroid-centroid distances of 3.613 Å. The oxygen atoms of the two DMSO, of which one solvent is found disordered, are engaged in strong O \cdots H-N



Scheme 1. Schematic representation of the synthesis of the proligands H₄L¹ and H₄L².

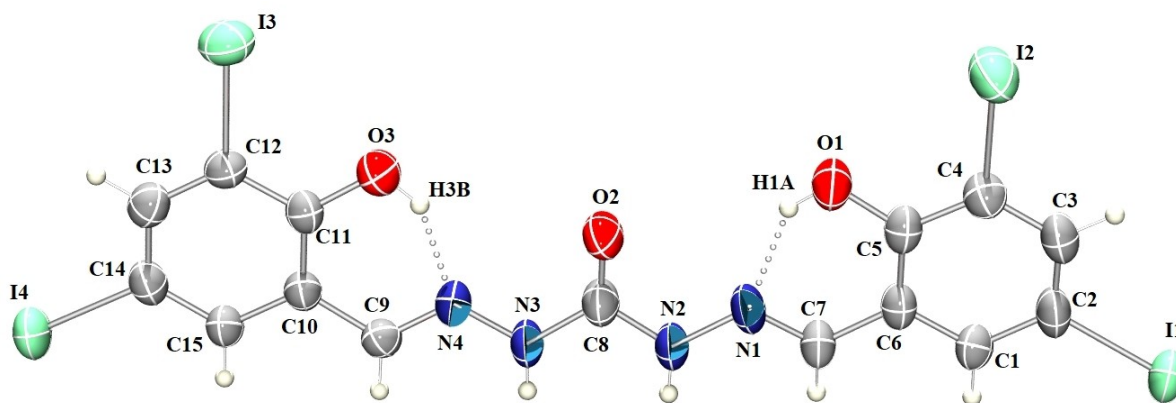


Figure 1. ORTEP diagram of H_4L^1 in 50% probability ellipsoids, showing intramolecular hydrogen bonds. DMSO solvent molecules are omitted for clarity.

hydrogen bonding, while the weaker intermolecular hydrogen bonding between $C16-H16B \cdots O2$ and $C17-H17C \cdots O3$ are mutually complementing and plays an important role in the crystal structure packing.^[54] Interestingly, a halogen bond interaction is found between $I4 \cdots O4$ at a distance of 3.435(5) Å, which plays a key role in the 1D supramolecular network formation interconnected through the hydrogen bonding involving $N2-H2 \cdots O4$ (Figure 2).

Spectral features of the compounds

IR spectrum of the proligand H_4L^1 exhibited bands in the region 1704 cm^{-1} (DFT calculated 1834 cm^{-1}) attributed to $\nu(C=O)$ stretching vibrations, suggesting its existence in its keto form and is confirmed from the crystal structure. The $\nu(N-H)$ bands appear at 3410 cm^{-1} (calculated 3503 cm^{-1}) and 3420 cm^{-1} (calculated 3477 cm^{-1}) respectively for H_4L^1 and H_4L^2 (Figure S4). Also, a band at 1260 cm^{-1} (calculated 1293 cm^{-1}) assigned to $\nu(C=S)$ and the absence of $\nu(S-H)$ band in the region of 2570 cm^{-1} indicating that the proligand H_4L^2 remains as the thione tautomer in the solid state.^[34] Strong bands

appeared at 1628 (calculated 1678) and 1630 cm^{-1} (calculated 1668 cm^{-1}) for the proligands H_4L^1 and H_4L^2 respectively are attributed to azomethine $\nu(C=N)$, while the bands at 3415 (calculated 3418) and 3423 cm^{-1} (calculated 3437 cm^{-1}) indicates the presence of free $\nu(O-H)$. The bands observed at 1159 (calculated 1210) and 1152 cm^{-1} (calculated 1219 cm^{-1}) correspond to $\nu(N-N)$ and at 1343 (calculated 1475) and 1336 cm^{-1} (calculated 1476 cm^{-1}) are attributed to $\nu(C-O)$ of the proligands H_4L^1 and H_4L^2 respectively. Since the compounds were optimized in the gas phase and not involving hydrogen bonding and other noncovalent intermolecular interactions, the DFT calculated vibrational frequencies are normally higher than that of the experimental solid state IR spectra.^[32]

The solution phase electronic spectra of the proligands H_4L^1 and H_4L^2 ($0.5 \times 10^{-4} \text{ M}$) were recorded as DMF solutions (Figure 3a). The carbohydrazone H_4L^1 shows bands at 508 ($\epsilon = 2200 \text{ M}^{-1}\text{cm}^{-1}$) and 448 nm ($3700 \text{ M}^{-1}\text{cm}^{-1}$) assigned as $n \rightarrow \pi^*$ transitions and the bands observed at 345 ($\epsilon = 15400 \text{ M}^{-1}\text{cm}^{-1}$) and 305 nm ($\epsilon = 22500 \text{ M}^{-1}\text{cm}^{-1}$) are attributed to $\pi \rightarrow \pi^*$ transitions. Similarly, the sulfur analogue H_4L^2 displayed four bands at 502 ($\epsilon = 4900 \text{ M}^{-1}\text{cm}^{-1}$), 430 ($\epsilon = 11700 \text{ M}^{-1}\text{cm}^{-1}$), 360

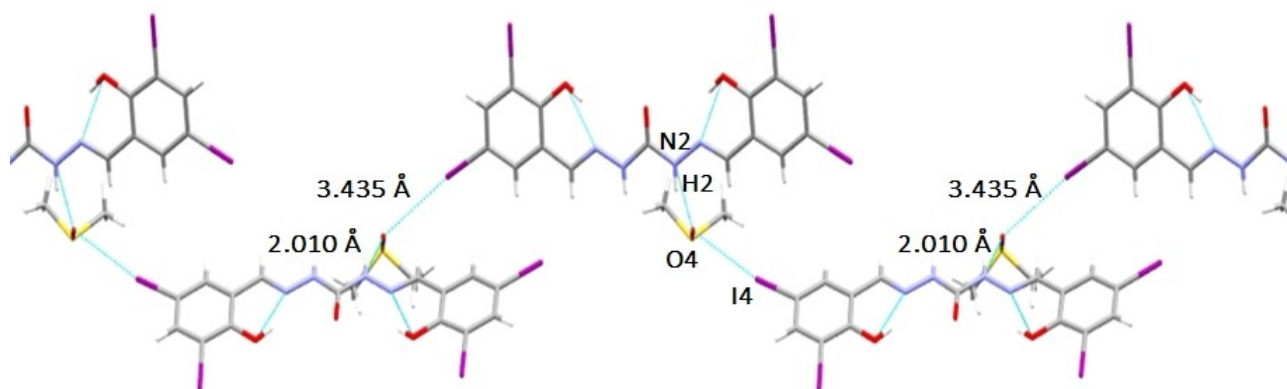


Figure 2. Formation of 1D chain due to halogen bonding and hydrogen bonding interactions in the supramolecular network of the proligand H_4L^1 (disordered DMSO is removed for clarity).

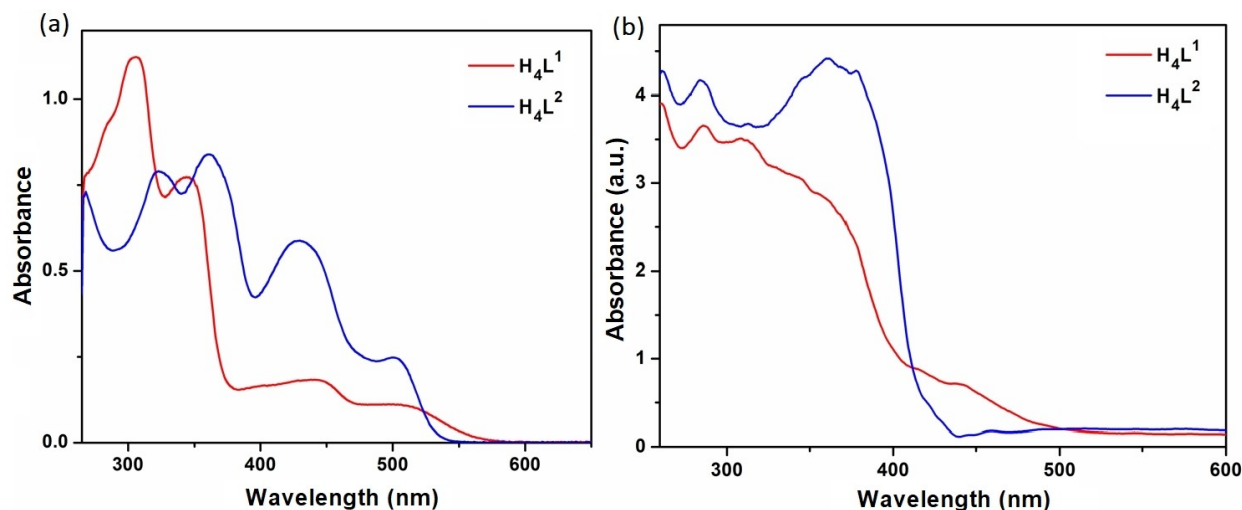


Figure 3. Solution state (a) and solid state (b) UV-Vis spectra of the proligands H_4L^1 (red) and H_4L^2 (blue).

($\epsilon = 16700 \text{ M}^{-1}\text{cm}^{-1}$) and 323 nm ($\epsilon = 15800 \text{ M}^{-1}\text{cm}^{-1}$), which are characteristics of $n \rightarrow \pi^*$ and $\pi \rightarrow \pi^*$ transitions. The solid-state electronic spectrum of H_4L^1 shows peaks at 286, 312, 345 and 446 nm, while that of H_4L^2 shows peaks at 283, 360, 377 and 426 nm respectively (Figure 3b). The band gap (E_g) of the proligands were determined experimentally using Kubelka-Munk graph plotted with $(F(R)h\nu)^2$ versus photon energy ($h\nu$), where $F(R)$ is Kubelka-Munk function. The direct band gap energy was found to be 2.61 and 2.90 eV for H_4L^1 and H_4L^2 respectively (Figure S5). These compounds are showing an unusual behavior in terms of the band gap and visible light absorption of (thio)carbohydrazones. So far reported similar carbohydrazones and thiocarbohydrazones all exhibited a lower band gap for thiocarbohydrazones, which is evidenced by their colors or visible light absorption wavelengths. This is because $C=S$ π interactions are generally weaker compared to $C=O$ π interactions and the lesser ionization potential of sulfur compared to oxygen.^[33,34] In studies, in general, thiocarbohydrazones are colored (yellow) compared to colorless carbohydrazones; but here the carbohydrazone H_4L^1 has absorbance in the visible region, brighter yellow in color, and shows lower band gap energy compared to the thiocarbohydrazone analogue H_4L^2 , which is pale yellow in daylight. This is attributed to strong solid state aggregation in the carbohydrazone H_4L^1 and is probably supported by strong $I_4 \cdots O_4$ type halogen bonding interactions along with intermolecular hydrogen bonding interactions involving carbonyl oxygen, which is revealed by the crystal structure study of H_4L^1 .

Aggregation induced emission (AIE) features

The solution state emission profile of both the proligands were recorded in DMF. The proligand H_4L^1 was excited at (λ_{ex}) 345 nm and it exhibited emission maximum at (λ_{em}) 556 nm, whereas the proligand H_4L^2 exhibited emission maximum at 539 nm when photoexcited at a wavelength of 370 nm. The

photoluminescence maximum of the proligand H_4L^1 in its solid state was observed at 614 nm by exciting at 345 nm. Here an orange emission with redshift of 58 nm was observed compared to that of its solution state spectrum. Similarly, the solid state maximum emission wavelength of the proligand H_4L^2 was shifted to 555 nm with a redshift of 16 nm, compared to its solution phase behavior, when it is excited at 360 nm, and a yellow emission was observed. Solution state and solid state emission spectra of the proligands with photographs under daylight and UV light are presented in Figure 4.

Aggregation induced emission luminogens (AIEgens) are a class of materials that are weakly or non-emissive when they are dissolved in good solvents, but emit particularly strong fluorescence when they are aggregated or in the solid state.^[1,6] Here, to investigate the emission behavior in the solid state, the aggregation properties of the proligands have been studied in DMF/water binary mixtures, and different water volumetric fractions (f_w) were recorded (Figure 5a and 5b). As the compounds are insoluble in water, molecules are aggregating in the binary mixture by the addition of water. The corresponding optical images represent the AIEE of H_4L^1 and ACQ of H_4L^2 under UV light as given in Figures 5c and 5d, respectively.

The PL intensity increases for the proligand H_4L^1 along with a slight blue shift by the addition of water, the trend continuous till $f_w = 30\%$. Interestingly, above $f_w = 30\%$, the compound exhibited dual emission peaks along with an increase in the PL intensity till $f_w = 60\%$, and then the intensity decreased further, and these emission changes can be attributed to the aggregation induced effect. Also, with the increase in the emission intensity upon gradual addition of water into the DMF, the fluorescence becomes gradually stronger and observed an AIEE. Contrary, the proligand H_4L^2 exhibits a decrease in the PL intensity along with a slight blue shift until $f_w = 40\%$ and shows a slight redshift further. But the fluorescence emission here is becoming weaker due to ACQ. AIEE in H_4L^1 compared to H_4L^2 may mainly be attributed to

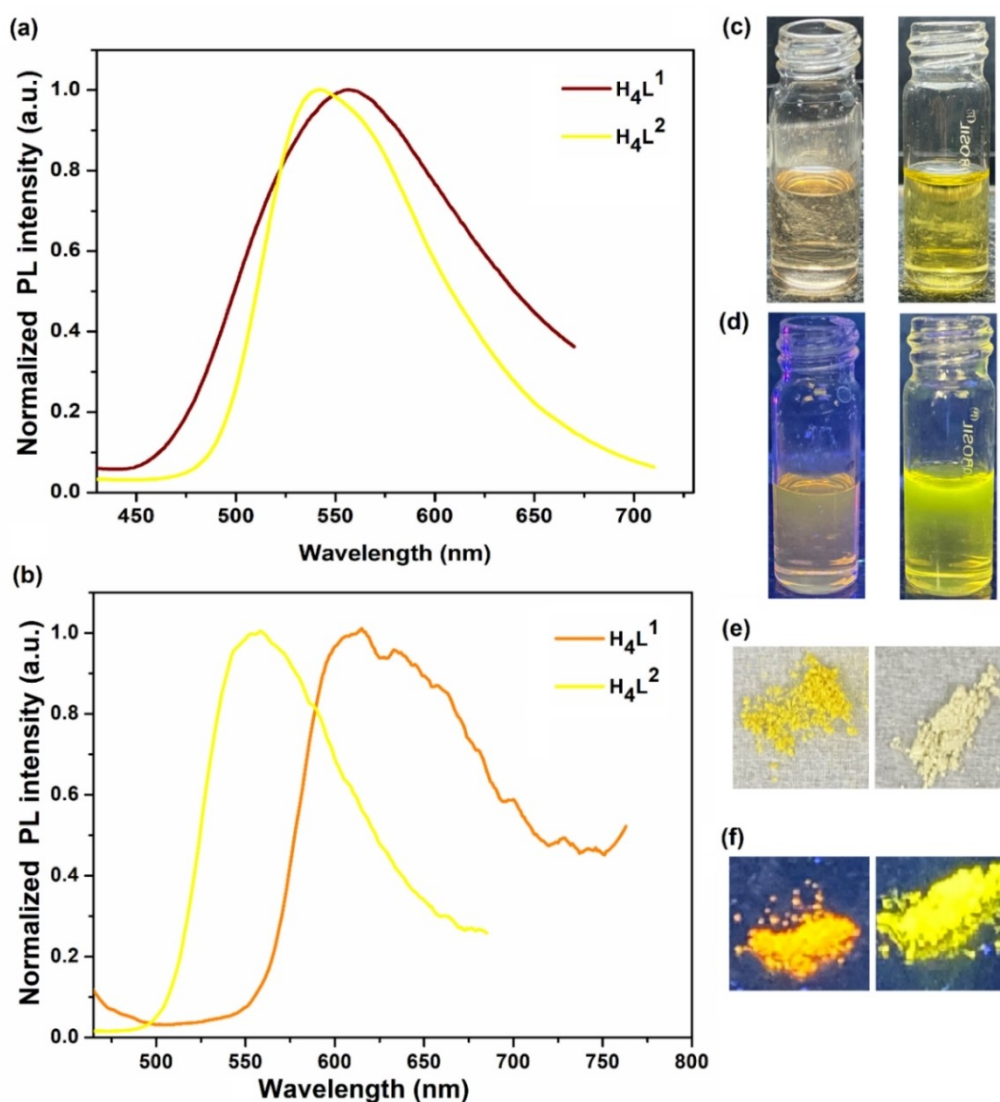


Figure 4. Solution state (a) and solid state (b) emission spectra of the proligands H_4L^1 and H_4L^2 , solution state optical images under daylight (c) and UV light (d), solid state optical images under daylight (e) and UV light (f) of the proligands H_4L^1 and H_4L^2 respectively.

restriction of intramolecular rotation^[55] due to strong I...O type halogen bonding and strong O...H-N type hydrogen bonding intermolecular interactions. Such noncovalent interactions would be stronger than possible mutual π ... π stacking interactions and thereby blocks nonradiative pathways *via* structural restriction, which leads to radiative emission enhancement. The absence of similar strong intermolecular interactions for H_4L^2 may reinforce π ... π stacking association, which enhances nonradiative pathways for exciton relaxation and leads to ACQ.

The UV-Vis spectra of the proligands (50 μ M) with different water fractions have also been recorded and are shown in Figure 6. The proligand H_4L^1 shows four major absorption peaks in dilute DMF solution. As the water fraction (f_w) increases to (50–500 μ L), the intensity of the peaks at \sim 508, \sim 445 and \sim 345 nm disappears gradually with a slight blueshift, and a new peak forms with an increase in intensity at \sim 394 nm.

Similarly, for H_4L^2 , the peaks at \sim 502 and \sim 430 nm are slightly blueshifted and disappear gradually by adding different water fractions (f_w), and are attributed due to aggregation induced effect.^[56]

Hirshfeld surface analysis of H_4L^1

The Hirshfeld surface (HS) analysis helps to quantify the intermolecular interactions in the crystal structure.^[57,58] The HS and related 2D finger plots of the proligand H_4L^1 were determined using crystal explorer 17.5^[59] software based on the results of SCXRD. HS was generated after modelling the structure by manually removing the minor components of the disordered DMSO molecule and putting full occupation on the major components in the CIF. The normalized contact distance d_{norm} function is the combination of the distance from HS to the nearest molecule internal to the surface (d) and the

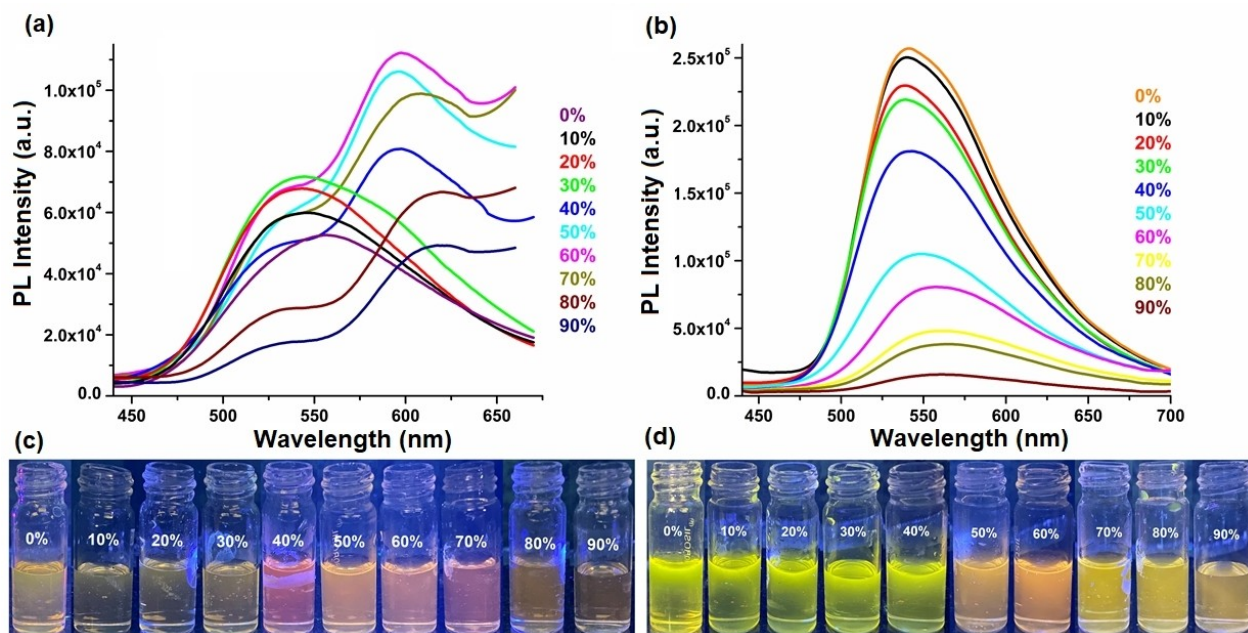


Figure 5. Fluorescence emission spectra of (a) H₄L¹ (excitation at 345 nm) and (b) H₄L² (excitation at 370 nm) in DMF/H₂O binary mixture. The percentage represents the volumetric fraction (f_v) of H₂O. Optical images represent the AIEE of (c) H₄L¹ and ACQ of (d) H₄L² under UV light (excitation at 345 nm).

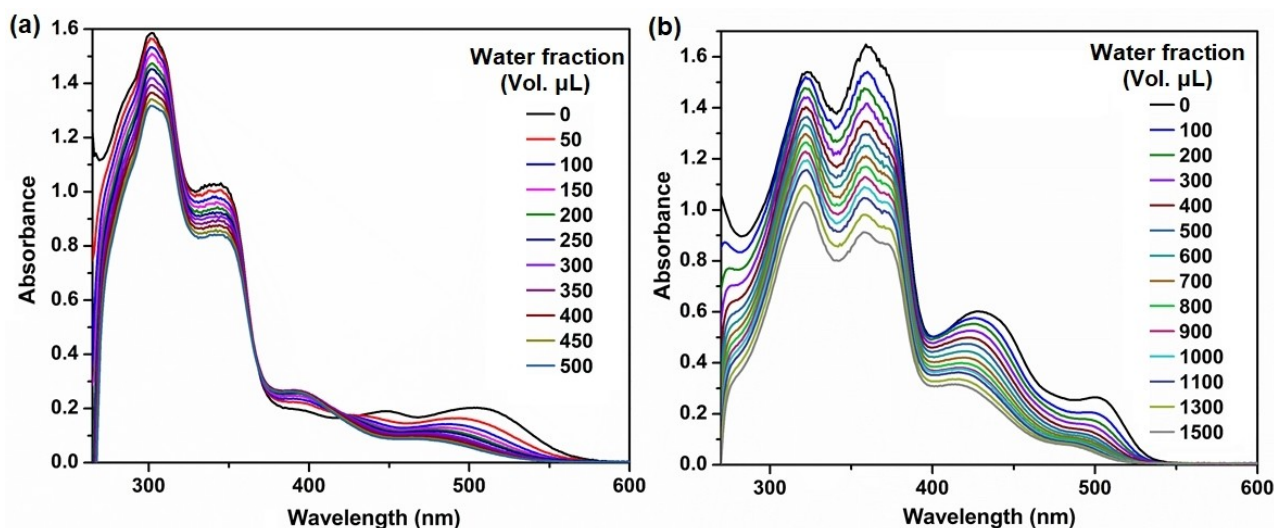


Figure 6. Absorption spectra of (a) H₄L¹ and (b) H₄L² in DMF/H₂O binary mixture. The compound in DMF taken as fixed (2000 μL) and added different volumetric fraction (f_v) of H₂O.

distance from HS to the closer molecule external to the surface (d_c). The blue region of the surface indicates the distances longer than the sum of van der Waals radii of the involved atoms, whereas white regions correspond to the contacts closer to van der Waals limit and red areas correspond to the contacts shorter than van der Waals limit.^[57]

The d_{norm} HS of the proligand shows intense red spots indicating the intermolecular hydrogen bonding regions. The HS of the proligand is mapped with the shape index function, which is used to examine the $\pi \cdots \pi$ stacking interactions of the

crystal structure. The pattern of red and blue triangles indicates the presence of $\pi \cdots \pi$ interactions between the phenylene rings of the molecules. The d_{norm} and shape index mapped are presented in Figure 7. The 2D fingerprint plot^[60] of the compound reveals the nature and type of all intermolecular interactions of the molecule in the crystal lattice. The fingerprint plot indicates that H \cdots I/H \cdots H interactions, which contain 32.7% of HS area, have the highest contribution in the crystal packing relative to the other contacts. The relative contributions from H \cdots H (18.6%), C \cdots H/H \cdots C (11.5%) and O \cdots H/H

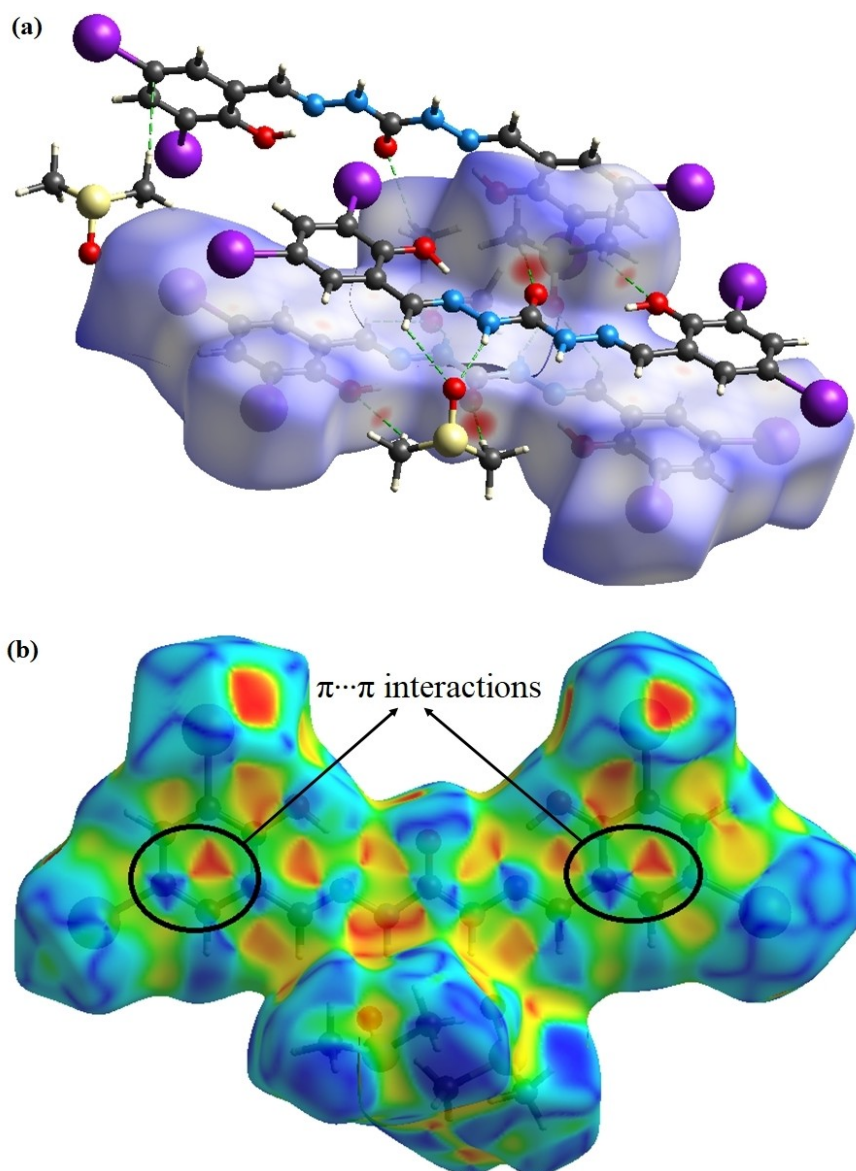


Figure 7. 3D Hirshfeld maps with (a) d_{norm} and (b) shape index of the proligand H_4L^1 .

···O (11.0%) interactions are the most significant. The C···H/H···C contacts are indicative of the significance of C–H···π interactions, which are relevant and reinforce the crystal packing. O···I/I···O interactions are a measure of halogen bonding interaction and are found relevant. C···C interaction covers 3.8% of the respective HSs, which is considered a measure of π···π interactions. Other weak interactions such as I···I and N···H/H···N contacts also contribute 3.3% and 3.0% to the HS area, respectively (Figure 8 and Figure S6).

Theoretical study of the proligands

Frontier molecular orbital (FMO) analysis

Computational study was performed to gain a molecular-level understanding of the spectral features and for FMO analysis. To

obtain the optimized molecular structures and to understand and compare the FMO energy gap, theoretical investigations were carried out for similar (thio)carbohydrazone ligands H_2L^3 , H_2L^4 , H_2L^5 and H_2L^6 using B3LYP/6-311G(d,p) basis set. Biscarbohydrazones H_2L^5 and H_2L^6 are the oxygen analogues of the bisthiocarbohydrazones H_2L^3 and H_2L^4 respectively. The relevant physical parameters obtained for the ligands and the proligands are listed in Table 2. The hard-soft range of the compounds were calculated by assuming $-E_{\text{HOMO}}$ as ionization energy and $-E_{\text{LUMO}}$ as electron affinity and these chemical descriptors^[61] are listed in Table S3.

The HOMO electron densities of both H_4L^1 and H_4L^2 are found distributed over the iodine and (thio)carbohydrazone moieties other than carbonyl/thiocarbonyl group, while the LUMO electron densities are distributed over the (thio)carbohydrazone moieties including carbonyl/thiocarbonyl

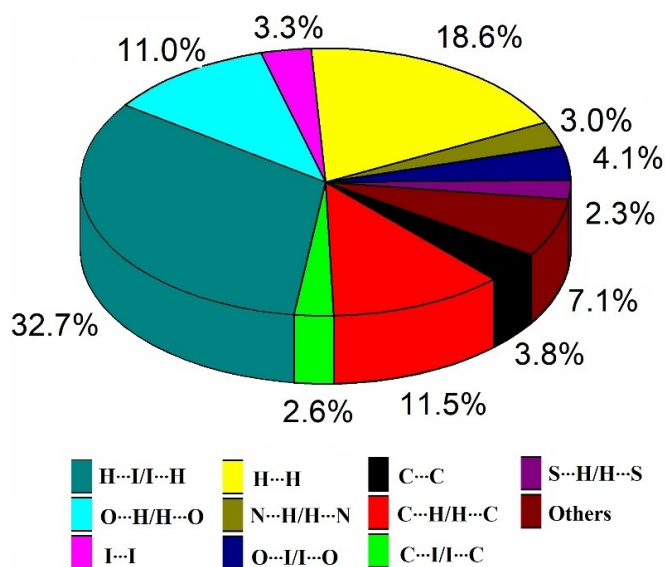


Figure 8. Pie diagram showing the different intermolecular contacts contributing to the total HS area of the proligand H_4L^1 .

group but other than NH moieties and iodine atoms. So, the possible HOMO to LUMO intramolecular charge transfer is mainly from iodine atoms to carbonyl/thiocarbonyl groups in these proligands. The negative energies of the HOMO, LUMO, and their neighboring orbitals of H_4L^1 , H_4L^2 , and the similar ligands reveal their molecular stability (Figures 9&10). The higher negative chemical potential ($\mu = -4.476$ eV) and low chemical hardness ($\eta = 1.827$ eV) indicate that the proligand H_4L^2 is comparatively softer ($\sigma = 0.274$ eV⁻¹) with higher polarizability than proligand H_4L^1 . Soft thiocarbohydrazone can easily donate electrons to soft acceptors and could be more reactive than that of harder ones like carbohydrazone H_4L^1 ($\eta = 1.950$ eV). The FMO energy gap of H_4L^1 and H_4L^2 calculated in the gas phase are found to be 3.900 and 3.655 eV respectively and are relatively closer. The carbohydrazones H_2L^5 (3.805 eV) and H_2L^6 (3.739 eV) have a large FMO energy gap compared to their sulfur analogues thiocarbohydrazones H_2L^3 (3.217 eV) and H_2L^4 (2.997 eV) respectively. Interestingly, the calculated experimental solid state band gap energy for the carbohydrazone H_4L^1 (2.61 eV) was found lower compared to that of the sulfur analogue H_4L^2 (2.90 eV) and is indicative of stronger molecular

association in the H_4L^1 solid lattice through intermolecular noncovalent forces.

Molecular electrostatic potential (MEP) surfaces

MEP maps are used to visualize the spatial electron density distribution over molecular surfaces.^[62] The positive and negative region of the electrostatic potential helps to predict the molecular shape, electrophilic and nucleophilic sites and various interaction possibilities between the molecules. MEP maps can detect the sites of interaction of small ligands to bind macromolecules, and are very useful in understanding the process of biochemical relevance, such as enzyme-substrate binding, catalysis, and drug-DNA binding.^[63] The blue colored region indicates a positive MEP associated with nucleophilic reactivity, while the red and yellow colors indicate a negative region of electrophilic attack. The green color indicates the neutral region of the compounds. The slight red color around the ketone part and yellow color over the phenolic oxygens of the proligand H_4L^1 indicates the region is prone to electrophilic attack. Similarly, the yellowish negative regions are associated with the lone pair of the electronegative thione and phenolic oxygens of H_4L^2 , indicating the Lewis base region and may have the ability to coordinate with metal centers or bind with electron deficient regions of proteins. Blue, on the other hand, shows the electron deficient region, mapped over the NH protons (Figure 11) is prone to nucleophilic regions of proteins.

ADMET studies

Absorption, Distribution, Metabolism, Excretion, and Toxicity (ADMET) properties of the compounds play an important role in the initial stage of drug discovery and development. Safety and lack of efficiency are the major reasons leading to drug failure, and it is necessary to find efficacious compounds with better ADMET properties.^[64] Here, to investigate the drug-likeness of the proligands, *in silico* ADMET prediction properties were carried out using SwissADME online software^[65] (for TPSA, n-ROTB, n-ON, n-OHNN, LogP, Lipinski's violations, and Veber's violation) and PreADMET online softwares^[66] (for Caco2 and HIA), and are summarized in Table 3. According to the Lipinski "Rule of five", a molecule cannot be orally activated if two or more rules are violated. It is assumed to be the compound having LogP_{o/w} (octanol/water partition coefficient) ≤ 5 , molecular weight (MW) ≤ 500 (H_4L^1 and H_4L^2 violate with > 500),

Table 2. DFT optimized physical parameters of the compounds.

Energy parameters (eV)	H_4L^1	H_4L^2	H_2L^3	H_2L^4	H_2L^5	H_2L^6
HOMO	-6.261	-6.303	-5.567	-5.531	-5.858	-6.093
HOMO-1	-6.339	-6.364	-5.707	-5.735	-6.214	-6.361
LUMO	-2.361	-2.648	-2.350	-2.554	-2.053	-2.353
LUMO + 1	-1.987	-2.060	-1.774	-2.226	-1.646	-2.104
$E_{\text{HOMO}} - E_{\text{LUMO}}: \Delta E$	3.900	3.655	3.217	2.977	3.805	3.739
Total Energy	-29062.43	-37850.41	-46906.41	-41819.57	-38118.30	-33030.37
Dipole moment (Debye)	8.141	8.154	5.933	7.743	4.753	6.500
Polarizability, α (a.u.)	347.291	382.398	385.336	357.064	348.111	322.201

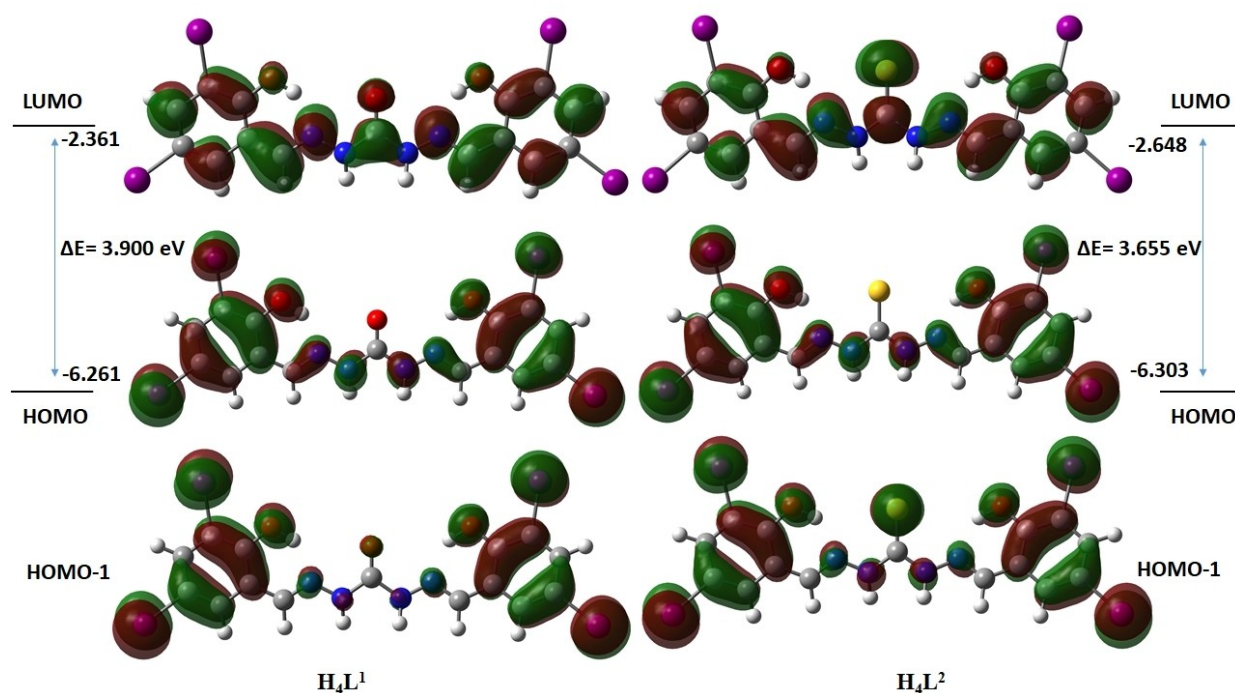


Figure 9. Relevant molecular orbitals of the proligands H_4L^1 and H_4L^2 in the gas phase.

Table 3. Physicochemical properties, lipophilicity and drug-likeness of the compounds.

Ligands	MW ^[a]	TPSA ^[b]	n-ROTB ^[c]	n-ON ^[d]	n-OHNH ^[e]	LogP ^[f]	L.V. ^[g]	V.V. ^[h]	Caco2 ^[i]	HIA ^[j]
H_4L^1	801.88	106.31	6	5	4	4.33	1	0	14.31	95.23
H_4L^2	817.95	121.33	6	4	4	4.92	1	0	19.58	95.27
H_2L^3	438.51	132.43	8	6	2	2.94	0	0	20.58	95.59
H_2L^4	384.46	106.65	6	4	2	3.56	0	0	20.55	96.49
H_2L^5	422.44	117.41	8	7	2	2.64	0	0	1.27	95.25
H_2L^6	368.39	91.63	6	5	2	3.03	0	0	6.77	95.41

Note. [a] MW: molecular weight (≤ 500 , expressed as g/mol), [b] TPSA: topological polar surface area (\AA^2), [c] n-ROTB: number of rotatable bonds, [d] n-ON: number of hydrogen bond acceptors (≤ 10), [e] n-OHNH: number of hydrogen bond donors (≤ 5), [f] LogP: logarithm of partition coefficient (≤ 5) of compound between n-octanol and water, [g] L.V.: Lipinski's violations, [h] V.V.: Veber's violation, [i] Caco-2: Caco-2 cell permeability (PCaco-2 (nm/s), < 4 : low, 4–70: middle, > 70 : high); [j] HIA(%): human intestinal absorption (0–20 = poor, 20–70 = moderate, 70–100 = good).

number of hydrogen bond donors ($n\text{-OHNH} \leq 5$), number of hydrogen bond acceptors ($n\text{-ON} \leq 10$) were more likely to exhibit favorable bioavailability.^[64,67] The human intestinal absorption has been predicted to be more than 95% for all the compounds (HIA = 95.23–96.49%). Also, All the compounds had middle cell permeability with Caco2 values in the range (6.77–20.58 nm/s) except H_2L^5 (1.27 nm/s).

Molecular docking

Docking with SARS-CoV-2 main protease

Molecular docking is a useful computational tool for drug design approaches to simulate the interaction between drug molecules and target proteins. SARS-CoV-2 belongs to the β -coronavirus family, whose proteins consisting of main protease (M^{pro}) or 3CL^{pro} is the potential drug targets responsible for the

viral replication.^[18,22] Recently, we have reported that 1,5-bis(2-benzoyl pyridine) thiocarbohydrazone and its Mn(II) complex are having better putative binding potentials against SARS-CoV-2 main protease.^[32] As an extension to that, the binding efficiencies of similar (thio)carbohydrazones H_2L^3 and H_2L^5 , H_2L^4 and H_2L^6 and the novel luminogens H_4L^1 and H_4L^2 are investigated in a comparative manner. The DFT optimized structures of the compounds H_2L^3 , H_2L^6 and the CIF file formats of H_2L^4 and H_2L^5 were used to identify their binding potentials with SARS-CoV-2 main protease (6Y2F). As part of drug repurposing approaches, antimalarial drugs such as CQ and its hydroxy analogue HCQ, the anti-Ebola drug remdesivir, etc. have been used as drugs for the treatment of covid-19.^[17,68] Darunavir, lopinavir, and ritonavir are also considered here as they were also identified as active at 6Y2F^[69] and the PDB files of these compounds were obtained from drug-bank online.

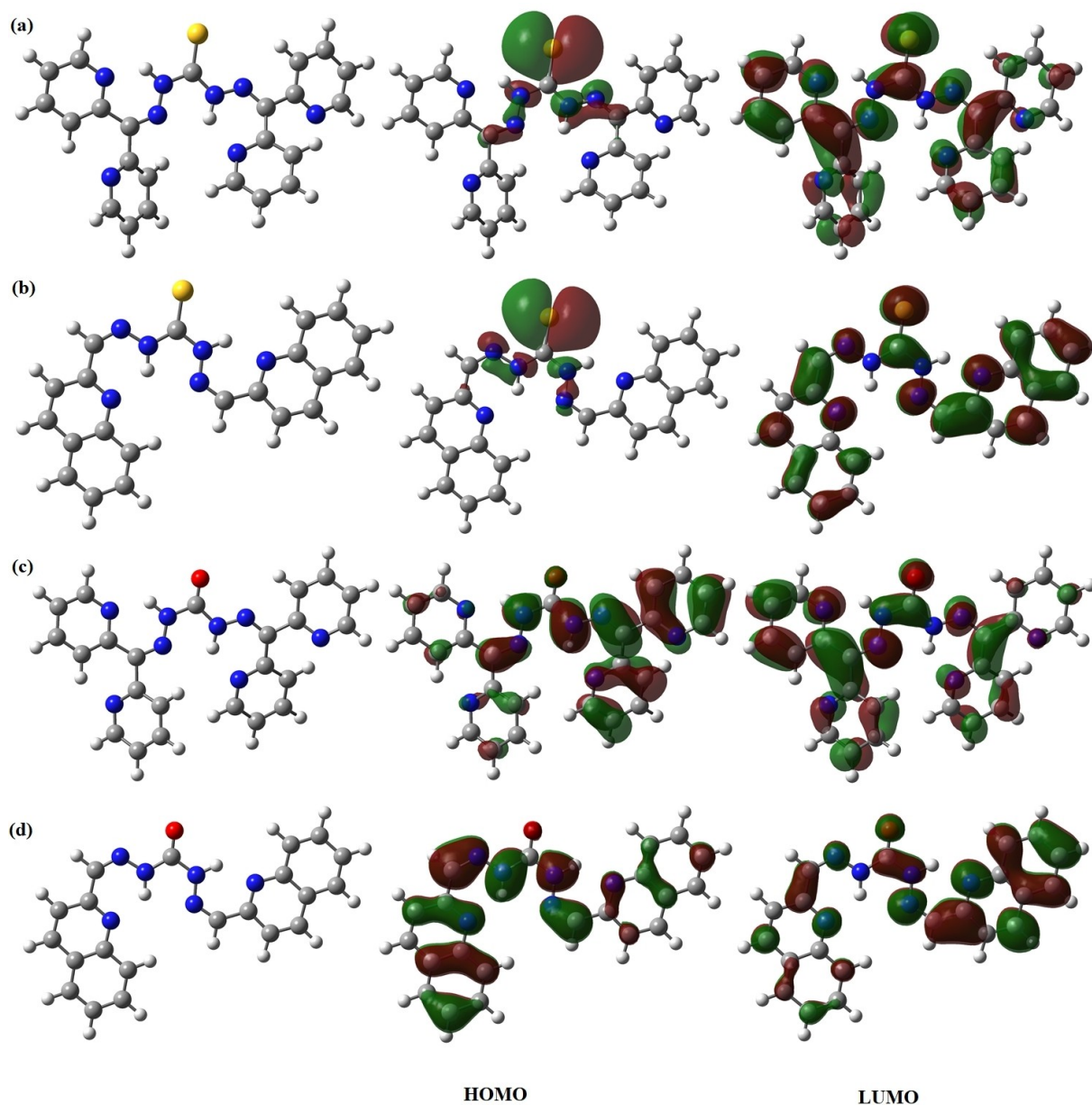


Figure 10. Optimized geometry, HOMO and LUMO representation of the ligands (a) H_2L^3 , (b) H_2L^4 , (c) H_2L^5 and (d) H_2L^6 .

The *in silico* docked poses and 2D interaction diagrams of the compounds with the target protein 6Y2F are given in Figures 12&S7 respectively. Docking energy, inhibition constant, and interactions of the ligands with 6Y2F are listed in Table 4. The docking energy of thiocarbohydrazone ligand H_4L^2 (−9.06 kcal/mol) is better than that of its oxygen analogue carbohydrazone H_4L^1 (−7.80 kcal/mol), cocrystal (−8.90 kcal/mol), CQ (−6.38 kcal/mol), HCQ (−6.69 kcal/mol), lopinavir (−8.10 kcal/mol), ritonavir (−8.97 kcal/mol), darunavir (−8.67 kcal/mol) and remdesivir (−8.32 kcal/mol) (Table S4). The thiocarbohydrazone H_4L^2 exhibit three conventional hydrogen bonding interactions with the active site residues GLU166(N), GLU166(O), PHE140(O), and other nonbonding interactions with THR-26, HIS-41, MET-49, CYS-145, HIS-164,

MET-165, GLU-166, and HIS-172. Furthermore, the binding energies of thiocarbohydrazone ligands H_2L^3 (−8.52 kcal/mol) and H_2L^4 (−8.81 kcal/mol) are better than those of their corresponding oxygen analogues H_2L^5 and H_2L^6 (−8.21 and −8.78 kcal/mol respectively). The halogen bond containing biomolecular compounds, in which the short distance halogen-electron rich atom (O, N, S) bonding interactions potentially stabilize the ligands bind to proteins and nucleic acids, have been reported to offer halogen bonds as a new tool for biomolecular drug design and engineering.^[70–72] Both the proligands H_4L^1 and H_4L^2 exhibit halogen bonding type interactions with the active site residues, though H_4L^1 possesses only weak bonding between iodine and ASP187(C) with a 3.584 Å bond distance. Interestingly, H_4L^2 having strong I...O

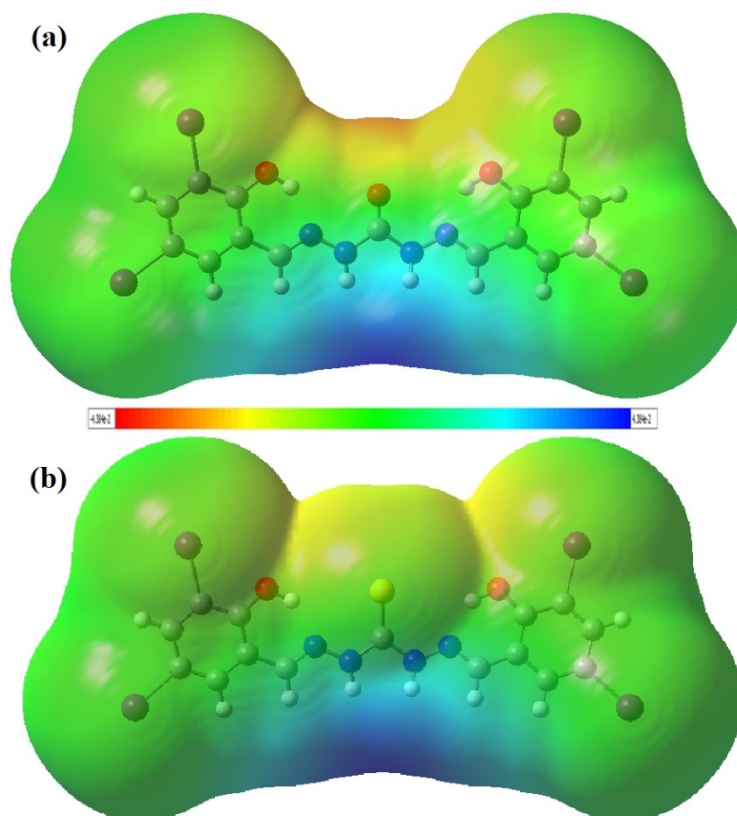


Figure 11. Molecular electrostatic potential maps of (a) H_4L^1 and (b) H_4L^2 .

Table 4. Docking energy, inhibition constant and interactions of the compounds with 6Y2F.

Compound	Docking energy (kcal/mol)	Inhibition constant (μM)	Interaction with amino acid residues	
			Hydrogen bonding	Residues involving hydrophobic and other interactions
H_4L^1	-7.80	1.93	GLY143(N) : N1 H(O3) : GLU166(O)	THR-26, HIS-41, MET-49, MET-165, ASP-187
H_4L^2	-9.06	0.2281	GLU166(N) : N1 S : PHE140(O) H(O1) : GLU166(O)	THR-26, HIS-41, MET-49, CYS-145, HIS-164, MET-165, GLU166, HIS-172
H_2L^3	-8.52	0.5676	H(N4) : HIS164(O) H(N4) : CYS145(SG)	HIS-41, MET-49, LEU-141, SER-144, CYS-145, MET-165,
H_2L^4	-8.81	0.3502	H(N5) : HIS164(O) H(N4) : HIS164(O)	HIS-41, CYS-145, HIS-163, MET-165, VAL-186
H_2L^5	-8.21	0.9635	H(N3) : HIS164(O) CYS145(N) : (O1) THR26(N) : N8	THR-25, LEU-141, ASN-142, CYS-145
H_2L^6	-8.78	0.3677	CYS145(SG) : N3 H(N5) : THR26(O) H(N3) : HIS164(O)	HIS-41, MET-49, CYS-145, HIS-163, MET-165, ARG-188, GLN-189

halogen bonding with THR26(O) with a distance of 3.411 Å is found very significant. The short and strong I...O interaction of H_4L^2 potentially stabilizes the ligand-enzyme binding. In all the tested compounds, the proligand H_4L^2 fits more perfectly at the active site of the target enzyme than the other molecules. The interactions of the active site residues with the iodine atoms on the phenylene ring along with the sulfur atom at the center of the thiocarbohydrazone H_4L^2 are crucial for exhibiting more

negative binding energy. The novel better active compounds H_4L^1 and H_4L^2 are luminogens with different aggregation induced emission features and could be considered as probable lead candidates against SARS-CoV-2.

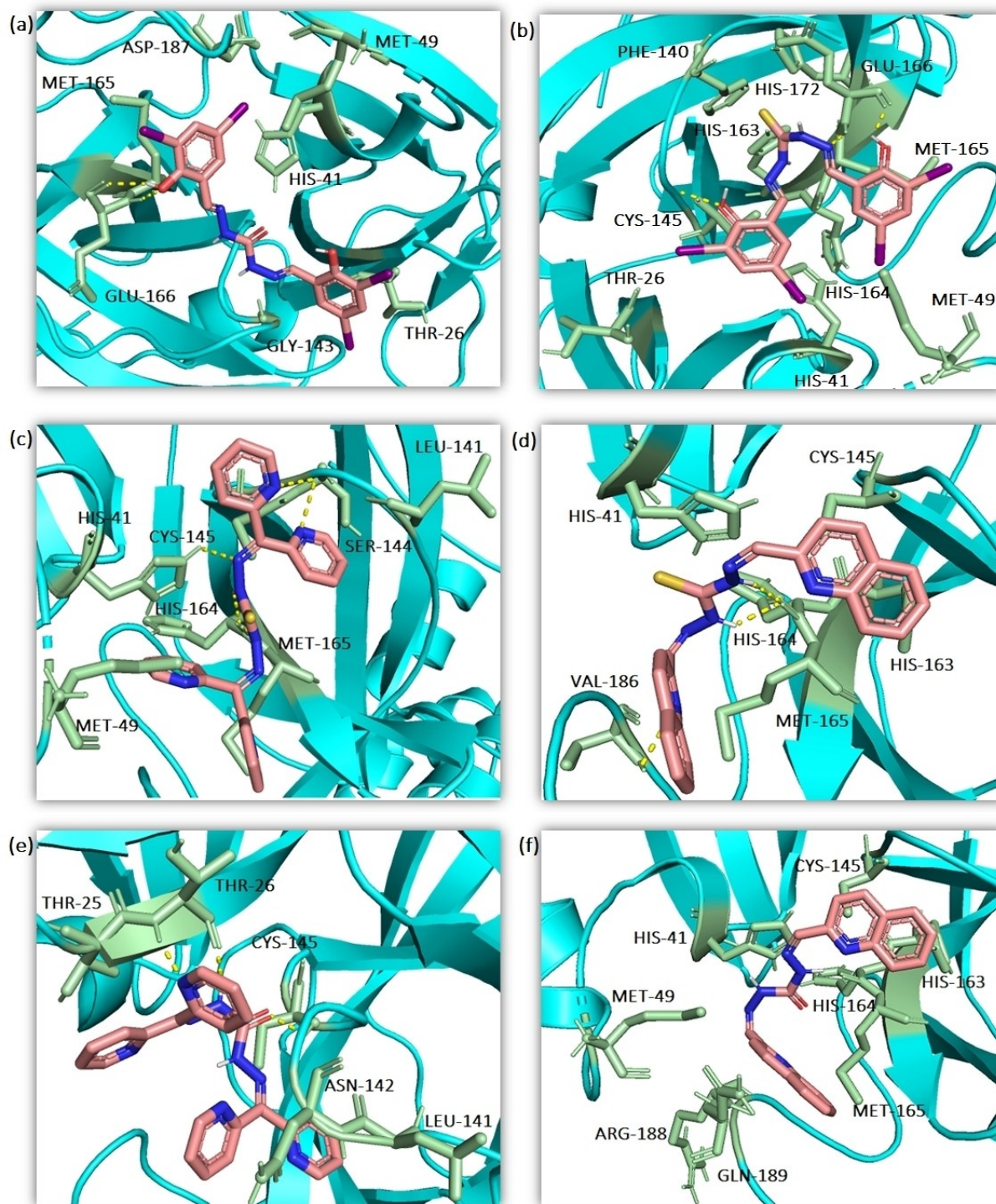


Figure 12. Interactions of the ligands (a) H_4L^1 , (b) H_4L^2 , (c) H_2L^3 , (d) H_2L^4 , (e) H_2L^5 and (f) H_2L^6 at the active site of SARS-CoV-2 main protease.

Docking of the luminogens with SARS-CoV-2 Spike protein

SARS-CoV-2 life cycle starts with their entry into the human cells and is mediated by the spike protein on the virus surface, which binds to the angiotensin-converting enzyme receptor-2 (ACE-2).^[73,74] Thus spike protein is also considered as one of the important targets for the development of SARS vaccines and

anti-viral drugs.^[73,74] AIE-based systems and modified AIEgens were used as bioprobes for the specific detection of infectious agents including viruses.^[75] Because of its important role in mediating viral entry into human cells, SARS-CoV-2 spike protein was selected as a target for bioprobe utility study.^[73] The virtual screening was performed against the SARS-CoV-2 spike glycoprotein (PDB ID: 6M0J, chain A) and the study aimed

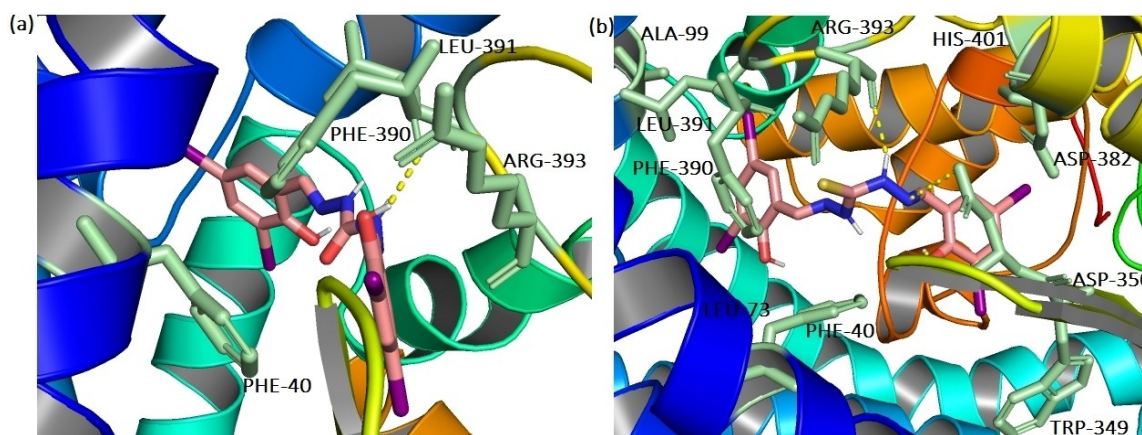


Figure 13. Docked conformations of (a) H_4L^1 and (b) H_4L^2 at the active site of SARS-CoV-2 spike protein.

to understand the most favorable binding of the fluorescent molecules (H_4L^1 and H_4L^2). The graphical representation of the proligands H_4L^1 and H_4L^2 interacting with different amino acid residues inside the SARS-CoV-2 spike protein along with hydrogen bonding and other intermolecular interactions are displayed in Figure 13 and Figure S8. The molecular docking calculations showed a good binding affinity with spike glycoprotein as evidenced by the docking energy of -7.34 and -5.88 kcal/mol for H_4L^1 and H_4L^2 respectively (Table 5). The virtual screening shows that both the fluorogenic molecules have different binding potentials, which may or may not affect the emission spectra and/or intensities and are to be evaluated experimentally. Better binding potential and AIEE feature suggest that the carbohydrazone luminogen H_4L^1 would be a good bioprobe for direct labelling of virus surface protein compared to the thiocarbohydrazone H_4L^2 .

4. Conclusion

Two new bioactive (thio)carbohydrazones H_4L^1 and H_4L^2 were synthesized and characterized. SCXRD and HS analysis of the proligand H_4L^1 have shown that strong inter- and intramolecular hydrogen bonding interactions, significant $C-H \cdots \pi$ and $\pi \cdots \pi$ interactions along with significant halogen bonding strengthen the packing of the molecules in the crystal lattice. DFT studies of the new compounds along with four similar

(thio)carbohydrazones were performed in a comparative manner. Band gaps of the compounds were estimated experimentally and are found to corroborate with theoretical calculations and indicate strong solid-state aggregation in the carbohydrazone H_4L^1 . Both the compounds exhibit fluorescence in both solid and solution phases and aggregation induced emission features. The carbohydrazone proligand H_4L^1 exhibits stronger fluorescence in its solid state due to AIEE, while the sulfur counterpart H_4L^2 displayed ACQ. All the six compounds exhibited efficient binding potentials with the enzyme 3CL^{pro} and the thiocarbohydrazone H_4L^2 showed excellent binding efficacy (-9.06 kcal/mol) among others and compared to CQ (-6.38 kcal/mol), HCQ (-6.69 kcal/mol), lopinavir (-8.10 kcal/mol), ritonavir (-8.97 kcal/mol), darunavir (-8.67 kcal/mol) and remdesivir (-8.32 kcal/mol). These results suggest that thiocarbohydrazones having iodine substituents may be useful drug candidates against SARS-CoV-2 main protease. Also, the luminogens H_4L^1 and H_4L^2 are found to exhibit good binding affinities toward SARS-CoV-2 spike protein with binding energy -7.34 and -5.88 kcal/mol respectively. As the detection sensitivity of nucleic acid assays or immunological assays is closely related to the performance of the luminescence probes, the novel better active carbohydrazone luminogen H_4L^1 opens up its usefulness as a bioprobe for the analysis of SARS-CoV-2 and for the monitoring of related biological processes.

Supporting Information Summary

1H -NMR and ^{13}C -NMR spectra, experimental and theoretical FT-IR spectra, Kubelka-Munk plots for band gap calculation, DFT calculated chemical reactivity parameters, molecular docking parameters and their 2D images have been provided along with bond lengths, bond angles, intermolecular interactions and Hirshfeld 2D fingerprint plots of the proligand H_4L^1 in the supporting information file. Deposition Number 2090512 (for H_4L^1) contains the supplementary crystallographic data for this paper. These data are provided free of charge by the joint Cambridge Crystallographic Data Centre and Fachinformationszentrum Karlsruhe Access Structures service.

Table 5. Docking energy and interactions of the luminogens with 6M0J.			
Compound	Docking energy (kcal/mol)	Interaction with amino acid residues	
		Hydrogen bonding	Residues involving hydrophobic and other interactions
H_4L^1	-7.34	H2(N2) : O1(H1 A) : PHE390(O)	PHE-40, PHE-390, LEU-391, ARG-393
H_4L^2	-5.88	H1(O1) : ARG393(O) H2(N2) : ASP350(O)	PHE-40, LEU-73, ALA-99, TRP-349, ASP-350, ASP-382, PHE-390, LEU-391, HIS-401

Acknowledgements

We thank the Sophisticated Analytical Instrumentation Facility (SAIF), Cochin University of Science and Technology, Kochi-22, India for analysis. EM is thankful to CUSAT for SMNRI grant (No. CUSAT/PL(UGC) A1/1112/2021) and MHKK is thankful to the Council of Scientific and Industrial Research, New Delhi, India (CSIR File No.09/239(0565)/2020-EMR-I) for the award of JRF.

Conflict of Interest

The authors declare no conflict of interest.

Data Availability Statement

The data that support the findings of this study are available in the supplementary material of this article.

Keywords: (Thio)carbohydrazone · X-ray diffraction · Aggregation-induced emission (AIE) · Molecular docking · SARS-CoV-2

- [1] C. Zhu, R. T. K. Kwok, J. W. Y. Lam, B. Z. Tang, *ACS Appl. Bio Mater.* **2018**, *1*, 1768–1786.
- [2] M. Mou, Y. Wu, Q. Niu, Y. Wang, Z. Yan, S. Liao, *Chem. Commun.* **2017**, *53*, 3357–3360.
- [3] Y. Zhang, D. Li, Y. Li, J. Yu, *Chem. Sci.* **2014**, *5*, 2710–2716.
- [4] Y. Kang, Z. Liao, M. Wu, S. Li, D. C. Fang, X. J. Zheng, L. P. Jin, *Dalton Trans.* **2018**, *47*, 13730–13738.
- [5] T. Han, Y. Hong, N. Xie, S. Chen, N. Zhao, E. Zhao, J. W. Y. Lam, H. H. Y. Sung, Y. Dong, B. Tong, B. Z. Tang, *J. Mater. Chem. C* **2013**, *1*, 7314–7320.
- [6] Y. Hong, J. W. Y. Lam, B. Z. Tang, *Chem. Commun.* **2009**, 4332–4353.
- [7] T. S. Reddy, J. Hwang, M. S. Choi, *Dyes Pigm.* **2018**, *158*, 412–419.
- [8] X. Gu, R. T. K. Kwok, J. W. Y. Lam, B. Z. Tang, *Biomaterials* **2017**, *146*, 115–135.
- [9] T. Luu, W. Li, N. M. O'Brien-Simpson, Y. Hong, *Chem. Asian J.* **2021**, *16*, 1027–1040.
- [10] L. Wang, Y. Wang, D. Ye, Q. Liu, *Int. J. Antimicrob. Agents* **2020**, *55*, 105948.
- [11] L. Chang, Y. Yan, L. Wang, *Transfus. Med. Rev.* **2020**, *34*, 75–80.
- [12] R. Lu, X. Zhao, J. Li, P. Niu, B. Yang, H. Wu, W. Wang, H. Song, B. Huang, N. Zhu, Y. Bi, X. Ma, F. Zhan, L. Wang, T. Hu, H. Zhou, Z. Hu, W. Zhou, L. Zhao, J. Chen, Y. Meng, J. Wang, Y. Lin, J. Yuan, Z. Xie, J. Ma, W. J. Liu, D. Wang, W. Xu, E. C. Holmes, G. F. Gao, G. Wu, W. Chen, W. Shi, W. Tan, *Lancet* **2020**, *395*, 565–574.
- [13] B. Udugama, P. Kadhiresan, H. N. Kozlowski, A. Malekjahani, M. Osborne, V. Y. C. Li, H. Chen, S. Mubareka, J. B. Gubbay, W. C. W. Chan, *ACS Nano* **2020**, *14*, 3822–3835.
- [14] J. Liu, R. Cao, M. Xu, X. Wang, H. Zhang, H. Hu, Y. Li, Z. Hu, W. Zhong, M. Wang, *Cell Discov.* **2020**, *6*, 6–9.
- [15] S. Keretsu, S. P. Bhujbal, S. J. Cho, *Sci. Rep.* **2020**, *10*, 1–14.
- [16] A. K. Singh, A. Singh, A. Shaikh, R. Singh, A. Misra, *Diabetes Metab. Syndr. Clin. Res. Rev.* **2020**, *14*, 241–246.
- [17] M. Pal, D. Musib, M. Roy, *New J. Chem.* **2021**, *45*, 1924–1933.
- [18] A. S. Achutha, V. L. Pushpa, S. Suchitra, *J. Proteome Res.* **2020**, *19*, 4706–4717.
- [19] T. Pillaiyar, M. Manickam, V. Namasivayam, Y. Hayashi, S. H. Jung, *J. Med. Chem.* **2016**, *59*, 6595–6628.
- [20] B. Elsässer, F. B. Zauner, J. Messner, W. T. Soh, E. Dall, H. Brandstetter, *ACS Catal.* **2017**, *7*, 5585–5593.
- [21] A. S. M. Al-Janabi, A. O. Elzupir, T. A. Yousef, *J. Mol. Struct.* **2021**, *1228*, 129454.
- [22] M. F. Hsu, C. J. Kuo, K. T. Chang, H. C. Chang, C. C. Chou, T. P. Ko, H. L. Shr, G. G. Chang, A. H. J. Wang, P. H. Liang, *J. Biol. Chem.* **2005**, *280*, 31257–31266.
- [23] K. Anand, J. Ziebuhr, P. Wadhvani, J. R. Mesters, R. Hilgenfeld, *Science* **2003**, *300*, 1763–1767.
- [24] D. W. Kneller, G. Phillips, H. M. O'Neill, R. Jedrzejczak, L. Stols, P. Langan, A. Joachimiak, L. Coates, A. Kovalevsky, *Nat. Commun.* **2020**, *11*, 7–12.
- [25] A. Aktaş, B. Tüzün, R. Aslan, K. Sayin, H. Ataseven, *J. Biomol. Struct. Dyn.* **2020**, 1–11.
- [26] L. Wang, B. B. Bao, G. Q. Song, C. Chen, X. M. Zhang, W. Lu, Z. Wang, Y. Cai, S. Li, S. Fu, F. H. Song, H. Yang, J. G. Wang, *Eur. J. Med. Chem.* **2017**, *137*, 450–461.
- [27] A. E. Gorbalenya, S. C. Baker, R. S. Baric, R. J. de Groot, C. Drosten, A. A. Gulyaeva, B. L. Haagmans, C. Lauber, A. M. Leontovich, B. W. Neuman, D. Penzar, S. Perlman, L. L. M. Poon, D. V. Samborskiy, I. A. Sidorov, I. Sola, J. Ziebuhr, *Nat. Microbiol.* **2020**, *5*, 536–544.
- [28] E. Manoj, M. R. P. Kurup, A. Punnoose, *Spectrochim. Acta Part A* **2009**, *72*, 474–483.
- [29] C. Bonaccorso, T. Marzò, D. La Mendola, *Pharmaceuticals* **2020**, *13*, DOI 10.3390/ph13010004.
- [30] R. S. Nair, E. Manoj, R. Thankappan, S. K. Chandrika, M. R. P. Kurup, P. Srinivas, *Mol. Carcinog.* **2017**, *56*, 1501–1514.
- [31] J. Haribabu, S. Srividya, D. Mahendiran, D. Gayathri, V. Venkatramu, N. Bhuvanesh, R. Karvembu, *Inorg. Chem.* **2020**, *59*, 17109–17122.
- [32] K. K. M. Hashim, E. Manoj, M. R. P. Kurup, *J. Mol. Struct.* **2021**, *1246*, 131125.
- [33] E. Manoj, M. R. P. Kurup, E. Suresh, *J. Chem. Crystallogr.* **2008**, *38*, 157–161.
- [34] E. Manoj, M. R. P. Kurup, H.-K. Fun, A. Punnoose, *Polyhedron* **2007**, *26*, 4451–4462.
- [35] E. Manoj, M. R. P. Kurup, H.-K. Fun, S. Chantrapromma, *Acta Crystallogr. Sect. E* **2005**, *61*, 4110–4112.
- [36] H. Hosseini-Monfared, R. Bikas, P. Mahboubi-Anarjan, S. Wenig Ng, E. R. T. Tiekink, *Zeitschrift für Anorg. und Allg. Chemie* **2014**, *640*, 243–248.
- [37] Y. Kaya, A. Erça, A. I. Koca, *J. Mol. Struct.* **2015**, *1102*, 117–126.
- [38] SMART and SAINT, Area Detector Software Package and SAX Area Detector Integration Program, Bruker Analytical X-Ray; Madison, WI, USA, **1997**.
- [39] G. M. Sheldrick, *Acta Crystallogr. Sect. C Struct. Chem.* **2015**, *71*, 3–8.
- [40] L. J. Farrugia, *J. Appl. Crystallogr.* **2012**, *45*, 849–854.
- [41] A. L. Spek, *J. Appl. Crystallogr.* **2003**, *36*, 7–13.
- [42] C. F. Macrae, P. R. Edgington, P. McCabe, E. Pidcock, G. P. Shields, R. Taylor, M. Towler, J. Van De Streek, *J. Appl. Crystallogr.* **2006**, *39*, 453–457.
- [43] K. Brandenburg, Diamond Version 3.2 g, Crystal Impact GbR, Bonn, Germany, 1997–2001., <http://www.crystalimpact.com/diamond>.
- [44] M. J. Frisch, G. W. Trucks, H. B. Schlegel, G. E. Scuseria, M. A. Robb, J. R. Cheeseman, G. Scalmani, V. Barone, B. Mennucci, G. A. Petersson, H. Nakatsuji, M. Caricato, X. Li, H. P. Hratchian, A. F. Izmaylov, J. Bloino, G. Zheng, J. L. Sonnenberg, M. Hada, M. Ehara, K. Toyota, R. Fukuda, J. Hasegawa, M. Ishida, T. Nakajima, Y. Honda, O. Kitao, H. Nakai, T. Vreven, J. A. Montgomery, J. E. Peralta, F. Ogliaro, M. Bearpark, J. J. Heyd, E. Brothers, K. N. Kudin, V. N. Staroverov, R. Kobayashi, J. Normand, K. Raghavachari, A. Rendell, J. C. Burant, S. S. Iyengar, J. Tomasi, M. Cossi, N. Rega, J. M. Millam, M. Klene, J. E. Knox, J. B. Cross, V. Bakken, C. Adamo, J. Jaramillo, R. Gomperts, R. E. Stratmann, O. Yazyev, A. J. Austin, R. Cammi, C. Pomelli, J. W. Ochterski, R. L. Martin, K. Morokuma, V. G. Zakrzewski, G. A. Voth, P. Salvador, J. J. Dannenberg, S. Dapprich, A. D. Daniels, O. Farkas, J. B. Foresman, J. V. Ortiz, J. Cioslowski, D. J. Fox, Gaussian 09, Revision A.1, Gaussian, Inc., Wallingford CT, **2009**.
- [45] R. Dennington, T. Keith, J. Millam, Shawnee Mission KS, GaussView, Version 5, Semichem Inc., **2009**.
- [46] A. D. Becke, *J. Chem. Phys.* **1993**, *98*, 5648–5652.
- [47] C. Lee, W. Yang, R. G. Parr, *Phys. Rev. B* **1988**, *37*, 785–789.
- [48] A. Allouche, *J. Comput. Chem.* **2012**, *32*, 174–182.
- [49] L. Zhang, D. Lin, X. Sun, U. Curth, C. Drosten, L. Sauerhering, S. Becker, K. Rox, R. Hilgenfeld, *Science* **2020**, *368*, 409–412.
- [50] J. Lan, J. Ge, J. Yu, S. Shan, H. Zhou, S. Fan, Q. Zhang, X. Shi, Q. Wang, L. Zhang, X. Wang, *Nature* **2020**, *581*, 215–220.
- [51] H. M. Berman, J. Westbrook, Z. Feng, G. Gilliland, T. N. Bhat, H. Weissig, I. N. Shindyalov, P. E. Bourne, *Nucleic Acids Res.* **2000**, *28*, 235–242.
- [52] BIOVIA and Dassault Systèmes, Discovery Studio Visualizer 19, Dassault Systèmes, San Diego, **2020**.

- [53] DeLano WL, The PyMOL Molecular Graphics System. De-Lano Scientific, San Carlos, CA, **2002**.
- [54] P. F. Rapheal, E. Manoj, M. R. P. Kurup, P. Venugopalan, *Chem. Data Collect.* **2021**, *33*, 100681.
- [55] S. Xu, Y. Duan, B. Liu, *Adv. Mater.* **2020**, *32*, 1–31.
- [56] G. Liu, M. Yang, L. Wang, J. Zheng, H. Zhou, J. Wu, Y. Tian, *J. Mater. Chem. C* **2014**, *2*, 2684–2691.
- [57] M. A. Spackman, D. Jayatilaka, *CrystEngComm* **2009**, *11*, 19–32.
- [58] J. J. McKinnon, M. A. Spackman, A. S. Mitchell, *Acta Crystallogr. Sect. B* **2004**, *60*, 627–668.
- [59] M. J. Turner, J. J. McKinnon, S. K. Wolff, D. J. Grimwood, P. R. Spackman, D. Jayatilaka, M. A. Spackman, *Crystal Explorer 17.5*, **2013**.
- [60] M. A. Spackman, J. J. McKinnon, *CrystEngComm* **2002**, *4*, 378–392.
- [61] T. Koopmans, *Physica* **1934**, *1*, 104–113.
- [62] J. S. Murray, P. Politzer, *Wiley Interdiscip. Rev.: Comput. Mol. Sci.* **2011**, *1*, 153–163.
- [63] M. Orozco, F. J. Luque, *Elsevier Sci. B. V.* **1996**, *3*, 181–218.
- [64] L. Guan, H. Yang, Y. Cai, L. Sun, P. Di, W. Li, G. Liu, Y. Tang, *MedChemComm* **2019**, *10*, 148–157.
- [65] A. Daina, O. Michielin, V. Zoete, *Sci. Rep.* **2017**, *7*, 1–13.
- [66] S. K. Lee, I. H. Lee, H. J. Kim, G. S. Chang, J. E. Chung, K. T. No, **2003**, 418–420. Blackwell Publishing, Massachusetts, USA.
- [67] D. Ngoc Toan, N. D. Thanh, M. X. Truong, D. Nghia Bang, M. Thanh Nga, N. Thi Thu Huong, *New J. Chem.* **2020**, *44*, 20715–20725.
- [68] M. E. A. Zaki, S. A. Al-Hussain, V. H. Masand, S. Akasapu, S. O. Bajaj, N. N. E. El-Sayed, A. Ghosh, I. Lewaa, *Pharmaceuticals* **2021**, *14*.
- [69] S. Pant, M. Singh, V. Ravichandiran, U. S. N. Murty, H. K. Srivastava, *J. Biomol. Struct. Dyn.* **2020**, *39*, 1–10.
- [70] M. R. Scholfield, C. M. Vander Zanden, M. Carter, P. S. Ho, *Protein Sci.* **2013**, *22*, 139–152.
- [71] M. Fourmigué, *Curr. Opin. Solid State Mater. Sci.* **2009**, *13*, 36–45.
- [72] P. Auffinger, F. A. Hays, E. Westhof, P. S. Ho, *PNAS* **2011**, *101*, 16789–16794.
- [73] A. Abdelaal Ahmed Mahmoud, M. Alkhatip, M. Georgakis, L. R. Montero Valenzuela, M. Hamza, E. Farag, J. Hodgkinson, H. Hosny, A. M. Kamal, M. Wagih, A. Naguib, H. Yassin, H. Algameel, M. Elayashy, M. Abdelhaq, M. I. Younis, H. Mohamed, M. Abdulshafi, M. A. Elramely, *Int. J. Mol. Sci.* **2021**, *22*, 1–13.
- [74] L. Du, Y. He, Y. Zhou, S. Liu, B. J. Zheng, S. Jiang, *Nat. Rev. Microbiol.* **2009**, *7*, 226–236.
- [75] K. Tanneeru, N. K. Bhatraju, R. S. Bhosale, S. K. Kalangi, *Front. Microbiol.* **2021**, *12*, 1–11.

Submitted: March 29, 2022

Accepted: July 7, 2022